Optimal Design of Compliant Mechanisms Using Functionally Graded Materials

Cian Conlan-Smith* · **Anurag Bhattacharyya** · **Kai A. James**

Abstract This research applies topology optimization to create feasible functionally graded complaint mechanism designs with the aim of improving structural performance compared to traditional homogeneous compliant mechanism designs. Converged functionally graded designs will also be compared with two-material compliant mechanism designs. Structural performance is assessed with respect to mechanical/geometric advantage and stress distributions. Two design problems are presented – a gripper and a mechanical inverter. A novel modified solid isotropic material with penalization (SIMP) method is introduced for representing local element material properties in functionally graded structures. The method of moving asymptotes (MMA) is used in conjunction with adjoint sensitivity analysis to find the optimal distribution of material properties. Geometric non-linear analysis is used to solve the mechanics problem based on the Neo-Hookean model for hyperelastic materials. Functionally graded materials (FGMs) have material properties that vary based on spatial position. Here, FGMs are implemented using two different resource constraints – one on the mechanism's volume and the other on the integral of the Young's modulus distribution throughout the design domain. Tensile tests are performed to obtain the material properties used in the analysis. Results suggest that FGMs can achieve the desired improvements in mechanical/geometric advantage when compared to both homogeneous and two-material mechanisms.

Keywords Topology Optimization · Complaint Mechanism Design · Functionally Graded Materials · Bio-Inspired Design · Geometric Non-Linearity.

1 Introduction

The main purpose of mechanisms is to transform an input motion, force, or energy at one location to an output at separate location. However, their most significant advantage is their ability to produce an output force or displacement which is higher than the input. This phenomenon is called mechanical (increasing force) or geometric (increasing displacement) advantage. Energy is conserved across the mechanism (excluding frictional losses) but if the output displacement is smaller than input displacement, the force at output must be greater than the input force to satisfy this conservation, or vice versa for geometric advantage. Traditionally this is achieved through the use of rigid-link mechanisms which incorporate rigid links connected at movable joints. Compliant mechanisms, however, transfer energy through the elastic deflection of structural members and the use of compliant joints. A comparison between these mechanisms is shown in Figure 1, represented by 4-bar linkages. Compliant mechanisms are light weight; require no lubrication; have a built-in restoring force due to their elastic nature; and experience less ware, friction and backlash compared to rigid link mechanisms. The methodology of using topology optimization for compliant mechanism design was first proposed by Sigmund [1] in 1997.

University of Illinois Urbana-Champaign,
Department of Aerospace Engineering,
Urbana, Illinois, United States.
E-mail: conlans2@illinois.edu*

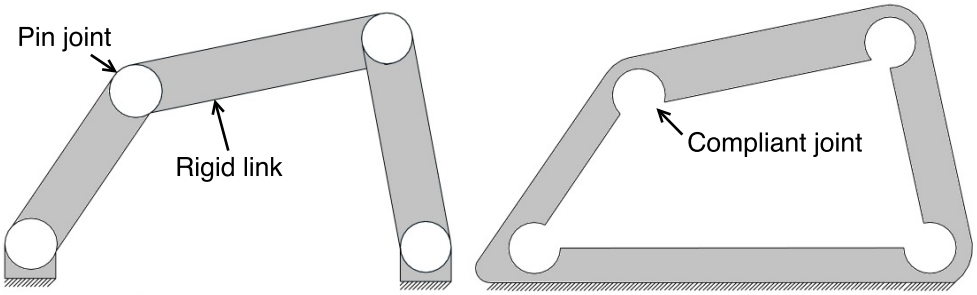

Fig. 1: A traditional mechanism with rigid links and movable pin joints (left), and a compliant mechanism with compliant joints (right).

In recent years compliant mechanisms have frequently been proposed for aerospace systems due to their advantages over traditional rigid-link mechanisms. As compliant mechanisms can be manufactured using fewer parts (usually one single part) they are lighter than their traditional counterparts. They are also easy to manufacture with modern 3D printing techniques, and do not require assembly. These advantages can have a large significance especially with the recent developments towards 3D printing in space [2], [3]. The ability to 3D print mechanisms and tools on board the International Space Station (or future bases on the Moon and Mars) will save substantially on the cost and time involved in transporting these devices from Earth. However, to achieve a broad-range of movement it is often necessary for compliant joints to be very thin. These thin members lead to increased localized stresses (stress concentrations) which cause limitations on the application of these mechanisms.

The motivation of this research is to seek more efficient compliant mechanism designs that can withstand higher load applications. We look to nature to solve this problem, more specifically to the human body. Throughout our body we have joints consisting of stiff bones, which act as structural members; and a combination of cartilage and synovial fluid between bones, which are compliant materials and allow movement. The joint mechanism receives power inputs from muscles and is held together by tendons (muscle to bone) and ligaments (muscle to muscle) [4]. Bones themselves consist of a graded type of material where their properties can vary depending on the position within the bone [5]. This wide range of different materials and material properties has been developed through millions of years of evolution to give us efficient joints throughout our body which act as mechanisms.

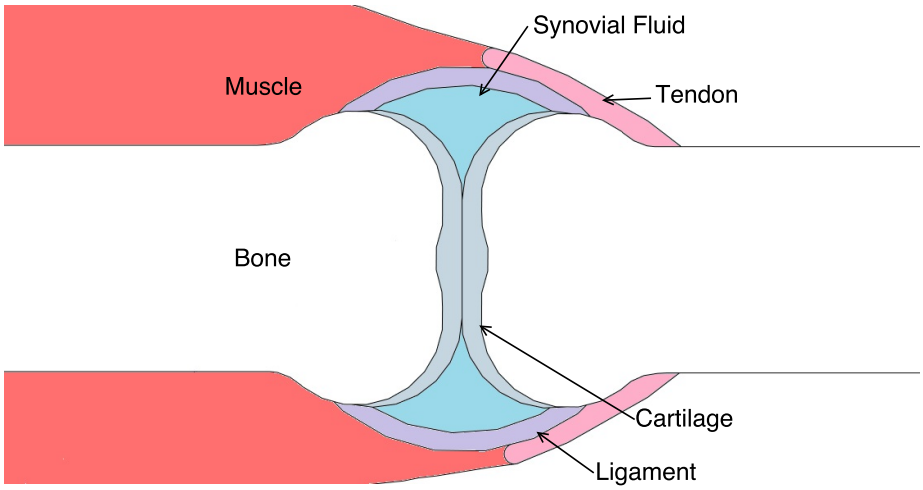

Fig. 2: Schematic of a human joint detailing different materials.

This combination of stiff and complaint materials allows extensive motion at our joints while also allowing high load transmissions. The assumption is that by varying the material properties in compliant mechanisms;

optimized solutions will concentrate a rubber-like complaint material at the joints while still using stiffer material for structural members, similar to the human joint. We hypothesize that by implementing heterogeneous materials, thus expanding the design space, improved geometric and mechanical advantages can be achieved, and thin structural members will be eliminated from the designs, improving stress distributions.

One method for achieving these designs is through implementing multiple discrete materials. However, when using multiple materials there is a distinct boundary between any two materials which can produce a stress concentration across the interface [6]. In contrast, functionally graded materials (FGMs) can produce a gradual change in material properties, such as Young's Modulus. FGMs are heterogeneous materials that produce a continuous gradation of material properties as a function of spatial position. This gradation is achieved through a continuous change in composition and microstructure with respect to location [7]. FGMs can be represented by mixing two materials with some distinctly different material property.

To date there has been little precedent in the literature for implementing FGMs into compliant mechanism design with the purpose of improving structural performance. However there has been significant work on multiple material compliant mechanisms to achieve this goal. Alonso et al. [8] used a sequential element rejection and admission (SERA) method to produce 2- and 3-material compliant mechanism designs. This procedure considers separate material models (one for each material in the design) in which elements can be rejected or admitted from the material models via separate criteria. Yin and Anathasuresh [9] also produced multi-material compliant mechanism designs using a peak function method. Bendsoe and Sigmund introduced a solid isotropic material with penalization (SIMP) method for multiple material topology optimization [10]. Subsequently Sigmund has produced other SIMP based formulations for multi-material compliant mechanism design [11] [12]. Similar SIMP based formulations were also adopted by Stegmann and Lund [13] where each element is assigned two design variables – one for topology optimization and another for material optimization. Gaynor and coauthors produced and prototyped 2-material complaint mechanism designs through PolyJet 3D printing [14]. Here, 2 different SIMP based methods were used to produce optimized designs which were prototyped and tested experimentally for comparison.

There are few examples in literature where FGMs are used in compliant mechanism design for different purposes. Carbonari et al. [15], [16] have modeled a functionally graded blend of piezoelectric and non-piezoelectric materials to produce actuators. These actuators have optimal topology and piezoelectric material distribution to produce an optimal overall performance. Similarly, Yin and Anathasuresh produced heterogeneous electro-thermal actuated complaint mechanisms consisting of blends of up to 3 materials using SIMP-based formulations [17]. There also examples of simultaneously optimizing topology and material gradation for structural applications. Xia [18] produced FGM beam structures using a level set method and interpreting any given point in the structure as a mixing ratio of two materials with differing modulus of elasticity. Stump et al. [19], introduced a method to design FGM distributions with a tailored von Mises stress field.

Compliant mechanisms experience large deformations and require elastic behavior to ensure functionality over a large number of cycles. Because of this compliant mechanisms can be achieved using hyperelastic materials which experience a nonlinear load-displacement relationship within their elastic range. There are a number of examples in the literature nonlinear finite element analysis is used for topology optimization [20], [21], [22]. Sigmund et al. has demonstrated the importance of nonlinear analysis in compliant mechanism design through a comparison with linear designs [21]. This paper shows how drastically optimized designs can change based on the finite element model, and even suggests a gain in performance as high as a factor of 2.5 can be achieved with non-linear vs. linear analysis. There are a number of hyperelastic models that can be used for this analysis as discussed in [23], [24], some recent example where these are implemented for topology optimization include [25], [26], [27], [28].

This paper will detail the methods used to generate a compliant mechanism designs using nonlinear analysis of hyperelastic materials with topology optimization. Section 2 details the finite element analysis methods and section 3 outlines the design problem and optimization approach. As all mechanical analysis is modeled on available materials, these materials are mechanically tested to achieve the material properties that will be used in simulations. Materials testing is outlined in section 4. Optimized designs and results are presented in section 5.

2 Mechanical Analysis

Because compliant mechanisms undergo large strains during operation conventional linear finite element analysis (FEA) is no longer suitable. Our analysis is conducted using FEA for geometrically nonlinear hyperelastic materials. A hyperleastic material is one where the material status can completely be describable with a given total strain [23]. In hyperelastic material models the potential energy function is represented as a function of deformation, and the stress can be obtained by differentiating the potential energy function with respect to deformation. Because of the elastic nature of these materials, the material model is independent of the deformation history, i.e. for the same final load the same deformation can be expected, and once the load is released the material will return to the unperturbed state. This section will detail the static response of hyperelastic materials based on the total Lagrangian formulation. There are two types of models for hyperelastic materials – mechanistic models, which are based off the underlying structure of the material; and phenomenological models, which are based off empirical observations. Mechanistic models (e.g. Neo-Hookean, and Arruda-Boyce) require independent material properties, such as Young's modulus and Poisson's ratio. Phenomenological models (e.g. Ogden, Mooney-Rivlin, and Yeoh) require parameters for curve fitting the material response to the model [29] [30]. For simplicity, we use the Neo-Hookean model as it requires only one material parameter [31]. We then require less experimental testing to obtain the material properties (compared to other mechanistic models) and additional curve fitting parameters required for phenomenological models. 4-node isoparametric quadrilateral elements will be used throughout the analysis.

A displacement control method is used where one non-zero displacement is specified. The aim is to solve for all unknowns in the problem, namely all unspecified displacements, and the magnitude of the external force required to create the specified non-zero displacement. This method will be explained in further detail later on. The total Lagrangian method assumes a continuous mapping between coordinates in the undeformed state, $\mathbf{X}$, and the current (deformed) state, $\mathbf{x}$. The deformation gradient, $\mathbf{F}$, can then be defined as,

$$\mathbf{F} = \frac{\partial \mathbf{x}}{\partial \mathbf{X}} \tag{1}$$

From Eqn. 1 it then holds that $\mathbf{F}$ is equal to the inverse of the derivative of $\mathbf{X}$ with respect to $\mathbf{x}$. This derivative can be calculated using element nodal coordinates of the undeformed state, $\mathbf{X}_e$, and the derivative of the shape function, $\mathbf{N}$, with respect to the deformed geometry $\mathbf{x}$.

$$\mathbf{F} = \left(\frac{\partial \mathbf{X}}{\partial \mathbf{x}}\right)^{-1} = \left(\left[\frac{\partial \mathbf{N}}{\partial \mathbf{x}}\mathbf{X}_e\right]^{\mathrm{T}}\right)^{-1} = \left(\mathbf{X}_e{}^{\mathrm{T}}\frac{\partial \mathbf{N}}{\partial \mathbf{x}}^{\mathrm{T}}\right)^{-1} \tag{2}$$

The right and left Cauchy-Green deformation tensors ($\mathbf{C}$ and $\mathbf{B}$ respectfully) can then be defined in terms of the deformation gradient.

$$\mathbf{C} = \mathbf{F}^{\mathrm{T}}\mathbf{F} \tag{3}$$

$$\mathbf{B} = \mathbf{F}\mathbf{F}^{\mathrm{T}} \tag{4}$$

The compressible Neo-Hookean model is then used to solve the mechanics problem. As mentioned previously the potential energy function can be used to compute stresses within hyperelastic materials. For isotropic materials the constitutive relation must be independent of the coordinate frame as the material properties are the same in all directions. This means that a strain component such as ε_{11} cannot be used for the constitutive relation since it is dependent on the coordinate system. Hence, the potential energy function is defined using Lamé constants and the right Cauchy-Green deformation tensor.

$$\Phi = \frac{1}{2}\lambda_0[\ln J]^2 - \mu_0 \ln J + \frac{1}{2}\mu_0[\mathrm{tr}(\mathbf{C}) - 3] \tag{5}$$

where J is computed as the determinant of the deformation gradient, F. The term tr($\mathbf{C}$) denotes the trace of the right Cauchy-Green deformation tensor. Eqn. 5 also utilizes the Lamé constants, μ_0 and λ_0, which can be represented in terms of the Young's modulus, E, and the Poison's ratio, ν. Materials testing is conducted to obtain values for E and ν (refer to section 4).

$$\mu_0 = \frac{E}{2(1+\nu)} \tag{6}$$

$$\lambda_0 = \frac{\nu E}{(1+\nu)(1-2\nu)} \tag{7}$$

The Second Piola-Kirchoff stress, $\mathbf{S}$, can now be calculated as twice the derivative of the potential energy function with respect to the right Cauchy-Green deformation tensor.

$$\mathbf{S} = 2\frac{\partial \Phi}{\partial \mathbf{C}} = \lambda_0[\ln J]\mathbf{C}^{-1} + \mu_0(\mathbf{I} - \mathbf{C}^{-1}) \tag{8}$$

The Second Piola-Kirchoff stress relates forces in the reference configuration (undeformed state) with areas also measured in the reference configuration. From here we can now evaluate the Cauchy stress, $\boldsymbol{\sigma}$, which will relate forces in the current configuration (deformed state) with areas in the current configuration. The Cauchy stress is defined as

$$\boldsymbol{\sigma} = \frac{1}{J}\mathbf{F}\mathbf{S}\mathbf{F}^{\mathrm{T}} \tag{9}$$

and using Eqn. 8, can be calculated as

$$\begin{aligned} \boldsymbol{\sigma} &= \frac{1}{J}\left[\lambda_0[\ln J]\mathbf{I} + \mu_0(\mathbf{F}\mathbf{F}^{\mathrm{T}} - \mathbf{I})\right] \\ &= \frac{1}{J}\left[\lambda_0[\ln J]\mathbf{I} + \mu_0(\mathbf{B} - \mathbf{I})\right] \end{aligned} \tag{10}$$

By rearranging the Cauchy stress to Voigt notation, $\bar{\boldsymbol{\sigma}}$ (3×1 in two dimensions), the internal force of a given element can be calculated by

$$\mathbf{f}_{int,e} = \int_{\Omega_e} \bar{\mathbf{B}}^{\mathrm{T}} \bar{\boldsymbol{\sigma}} d\Omega_e \tag{11}$$

where $\bar{\mathbf{B}}$ is the strain-displacement matrix containing spatial derivatives of $\mathbf{N}$ with respect to the deformed geometry, $\mathbf{x}$.

$$\bar{\mathbf{B}} = \overline{\frac{\partial \mathbf{N}}{\partial \mathbf{x}}} = \begin{bmatrix} \frac{\partial \mathrm{N}}{\partial \mathrm{x}}_{1,1} & 0 & \frac{\partial \mathrm{N}}{\partial \mathrm{x}}_{1,2} & 0 & \frac{\partial \mathrm{N}}{\partial \mathrm{x}}_{1,3} & 0 & \frac{\partial \mathrm{N}}{\partial \mathrm{x}}_{1,4} & 0 \\ 0 & \frac{\partial \mathrm{N}}{\partial \mathrm{x}}_{2,1} & 0 & \frac{\partial \mathrm{N}}{\partial \mathrm{x}}_{2,2} & 0 & \frac{\partial \mathrm{N}}{\partial \mathrm{x}}_{2,3} & 0 & \frac{\partial \mathrm{N}}{\partial \mathrm{x}}_{2,4} \\ \frac{\partial \mathrm{N}}{\partial \mathrm{x}}_{2,1} & \frac{\partial \mathrm{N}}{\partial \mathrm{x}}_{1,1} & \frac{\partial \mathrm{N}}{\partial \mathrm{x}}_{2,2} & \frac{\partial \mathrm{N}}{\partial \mathrm{x}}_{1,2} & \frac{\partial \mathrm{N}}{\partial \mathrm{x}}_{2,3} & \frac{\partial \mathrm{N}}{\partial \mathrm{x}}_{1,3} & \frac{\partial \mathrm{N}}{\partial \mathrm{x}}_{2,4} & \frac{\partial \mathrm{N}}{\partial \mathrm{x}}_{1,4} \end{bmatrix} \tag{12}$$

To keep structural equilibrium the internal and external forces must be balanced. This gives the global residual form as

$$\mathbf{R} = \mathbf{f}_{ext} - \mathbf{f}_{int} = \mathbf{0} \tag{13}$$

This residual equation gives rise to a nonlinear system of equations which are solved iteratively using a Newton-Raphson procedure to obtain the global vector of nodal displacements, $\mathbf{u}$. During each iteration the nodal displacements are updated by $\Delta\mathbf{u}$ (until convergence of Eqn. 13) using the linear system of equations

$$\mathbf{K}_{tan}\Delta\mathbf{u} = \mathbf{R} \tag{14}$$

The matrix $\mathbf{K}_{tan}$ is known as the tangent stiffness matrix and is formed by assembling element tangent stiffness matrices, $\mathbf{k}_{tan,e}$. The element tangent stiffness is calculated as a sum of a material and a geometric component as follows

$$\mathbf{k}_{tan,e} = \mathbf{k}^{geo}_{tan,e} + \mathbf{k}^{mat}_{tan,e} \tag{15}$$

$$\mathbf{k}_{tan,e} = \mathbf{I} \otimes \left(\int_{\Omega_e} \tilde{\mathbf{B}}^{\mathrm{T}} \boldsymbol{\sigma} \tilde{\mathbf{B}} d\Omega_e \right) + \int_{\Omega_e} \bar{\mathbf{B}}^{\mathrm{T}} \bar{\mathbf{D}} \bar{\mathbf{B}} d\Omega_e \tag{16}$$

where $\bar{\mathbf{D}}$ is the constitutive tensor which relating stress to strain (assuming plane strain) and is calculated via Eqn. 17, $\tilde{\mathbf{B}}$ is a special compact version of the strain displacement matrix, which retains only the nonzero entries from the original matrix, $\bar{\mathbf{B}}$. Note also that the operator $\otimes$, denotes the matrix outer product.

$$\bar{\mathbf{D}} = \begin{bmatrix} \lambda_0 + 2\mu_0 & \lambda_0 & 0 \\ \lambda_0 & \lambda_0 + 2\mu_0 & 0 \\ 0 & 0 & \mu_0 \end{bmatrix} \tag{17}$$

$$\tilde{\mathbf{B}} = \begin{bmatrix} \bar{\mathrm{B}}_{1,1} & \bar{\mathrm{B}}_{1,3} & \bar{\mathrm{B}}_{1,5} & \bar{\mathrm{B}}_{1,7} \\ \bar{\mathrm{B}}_{2,2} & \bar{\mathrm{B}}_{2,4} & \bar{\mathrm{B}}_{2,6} & \bar{\mathrm{B}}_{2,8} \end{bmatrix} \tag{18}$$

This method is further detailed in [23] and [24]. A displacement control method is used to solve the governing equation, $\mathbf{R} = 0$, and this method is outlined in [32]. The governing equation is solved to obtain nodal displacements and the magnitude of the applied force, θ through Eqn. 14. The external force used in Eqn. 13 is defined as

$$\mathbf{f}_{ext} = \theta \mathbf{f}_0 \tag{19}$$

where $\mathbf{f}_0$ is a sparse reference vector of size equal to the number of degrees of freedom and a unit value at the degree of freedom corresponding to the applied force.

3 Optimization Approach

3.1 Design Problem

This section details the topology optimization approach for two different design problems – a gripper, and a geometric inverter. The function of a gripper is to produce a mechanical advantage when gripping a workpiece, whereas an inverter aims to produce a displacement (or force) in the opposite direction to the input while producing some geometric (or mechanical) advantage. For the purpose of this analysis the gripper will produce a mechanical advantage while inverter produces a geometric advantage. The design domains of both problems are outlined in Figure 3. Due to the symmetry of the problem only half the domain is modeled. An input displacement, u_{in}, is prescribed at the left center of the design domains. At this input the nonlinear FEA code solves the resulting force to create this displacement. The output is specified at the right of the design domains and the structures are to be fixed at the top and bottom left corners of the domain. It is assumed that the gripper will act on a rigid workpiece and hence there will be no displacement at the output. Therefore, the output force will be equal to the negative of the reaction force at the output.

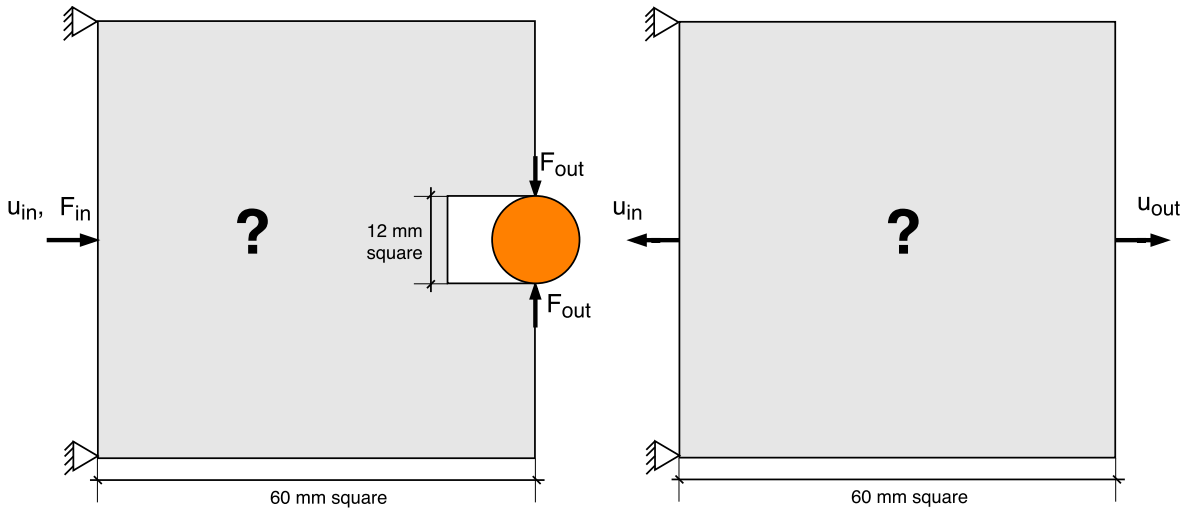

(a) Gripper design domain

(b) Inverter design domain

Fig. 3: The two design problems illustrating boundary conditions, inputs, outputs and dimensions.

The purpose of these designs is to maximize the mechanical (case a) or geometric (case b) advantage. The design problem is defined as follows

$$\begin{aligned}
\min_{x} \quad & : \quad g(\mathbf{u}(\boldsymbol{x}), \theta(\boldsymbol{x}), \boldsymbol{x}) \qquad = \frac{F_{out}}{F_{in}} \quad \text{(case a)} \\
& \qquad\qquad\qquad\qquad\quad = \frac{u_{out}}{u_{in}} \quad \text{(case b)} \\
\text{subject to} \quad & : \quad \int_{\Omega} \frac{M(\boldsymbol{x})}{M_0} d\Omega - \bar{M} \leq 0 \\
& : \quad C_{min} - C \leq 0 \\
& : \quad \mathbf{0} < \boldsymbol{x}_{min} \leq \boldsymbol{x} \leq \mathbf{1}
\end{aligned} \tag{20}$$

where g is the objective function which is equal to the ratio of input to output force (mechanical advantage) for the case of the gripper, and equal to the ratio of input to output displacement (geometeric advantage) for the case of the inverter. The objective function, g, is also subject to three constraints, each is described below.

1. The first constraint is on the resource, where $M(\boldsymbol{x})$ can be either the local volume or Young's modulus, which are both a function of the independent variables, i.e. a volume or modulus constraint is used – these constraints will be described in more detail further on. M_0 is the maximum value of M that is physically possible for the entire design domain, Ω. The ratio of $M(\boldsymbol{x})$ to M_0 is summed over Ω to give the resource fraction (volume or modulus fraction, refer to Eqn's 24 and 25). This ratio must be less than or equal to some user prescribed allowance, $\bar{M}$. Note also that the volume and modulus fractions are equal for the homogeneous case as the Young's modulus is constant for each element.
2. The second constraint is a compliance constraint which is imposed at the input for the gripper problem and the output for the inverter problem. This constraint ensures that there is a continuous chain of material between the point of application and the boundary conditions. Because the objective function is a ratio, it can continuously be minimized by lowering the output (for positive g) or input (for negative g), which in-turn prompts optimizer to solve this irregularity by reducing element densities at input/output locations. By ensuring some level of stiffness at the input/output locations (i.e. not void), the force must be large enough to overcome the resistance produced. Alternatively a minimum value constraint can be imposed on the input force for the gripper or output displacement for the inverter, but this will not necessarily guarantee the continuous chain of material as elements can still be pushed to void.
3. The final constraint is to keep each material density between zero and one. However, by specifying a minimum material density of zero the algorithm can diverge at Eqn. 2 as $\mathbf{F}$ is calculated by inverting a multiple of the shape function derivative. This derivative is calculated using the Jacobian matrix which will be singular if it is formed from elements of zero stiffness. To cope with this a minimum material density value, $\boldsymbol{x}_{min}$, is selected to be close enough to zero so that void regions have minimal impact in FEA results, but not too small that the non-linear solution procedure diverges. Note that this method is used in the homogeneous case only. For the functionally graded case the SIMP method is defined differently to cope with this problem (refer to Eqn. 22).

3.2 Discretization

The entire design domain is discretized into finite elements, where each element has a material density, $\boldsymbol{x}$. The material density is used as a parameter to determine which elements should be included in the design, and which should be excluded. The goal is to achieve a clear 1-0 structure at convergence where the element, e, is a part of the structure if its material density, x_e, is equal to 1 and void for x_e equal to 0 (or x_{min} for the homogeneous case). To produce a clear converged solution the material density for the elements must be forced to either 1 or 0. This is achieved using the SIMP (solid isotropic material with penalization) method [33], [34]. This is a gradient based approach that penalizes the material properties that relate to the Young's modulus.

$$E_e = x_e^p E_0 \implies \lambda_e = x_e^p \lambda_0 \quad ; \quad \mu_e = x_e^p \mu_0 \tag{21}$$

In the above, the subscript e indicates that the property is specific to an element. The element density raised to the power of p, multiplied by the material property for a solid material gives the effective material property for the penalized material. The penalization parameter, p, must be greater than one and is usually chosen to be either 3 or 5. By penalizing intermediate material densities (raised to the power of p) a solid-void design is promoted during optimization. The resource fraction, introduced in Eqn. 20, is calculated via Eqn. 22 for the homogeneous case.

$$\int_\Omega \frac{M(\boldsymbol{x})}{M_0} d\Omega = \frac{1}{A_\Omega t x_{max}} \sum_{e=1}^{N_e} A_e t x_e = \frac{1}{N_e} \sum_{e=1}^{N_e} x_e \tag{22}$$

The domain is assumed to have a uniform thickness, t, and an area, A_Ω, consisting of N_e elements of area A_e. As all elements are of equal size, Eqn. 22 reduces to the sum of material densities divided by the number of elements, N_e. We implement an original SIMP-type formulation for representing the local element material properties in the FGM problem. This method is similar to those adopted in [12] and [13] where each element is assigned two design variables. The effective Young's modulus is evaluated as follows

$$E_e = E_{min} + x_{0,e}^p \big(E_l + x_{1,e}(E_u - E_l)\big) \tag{23}$$

where the subscript *min* denotes the minimum allowable modulus value, l and u denote the lower and upper modulus limits, $x_{0,e}$ is the material density of the element e and is penalized such that $x_{0,e} \in \{0,1\}$ for all e at a converged result. The second design variable, $x_{1,e}$, is the mixing ratio between upper and lower bounds of the Young's modulus, which is not penalized such that $0 \leq x_{1,e} \leq 1$, thus promoting an unbiased material distribution. The addition of the term E_{min} insures that there is some stiffness in the void regions, therefore $x_{0,min} = 0$ for the functionally graded case. Note that the mixing ratios, $\boldsymbol{x_1}$, are computational design variables and do not represent the physical mixing ratio between materials. The physical mixing ratio (for manufacture) will be determined based on the local Young's modulus in converged designs. Also note that in order to compare homogeneous and FGM mechanisms, the minimum modulus must be equal for the two cases i.e. $E_{min} = {x_{min}}^p E_0$. Eqn. 23 gives the effective Young's modulus for the FGM case, which is used as E in Eqn's 6 and 7 to calculate Lamé constants. When a volume constraint is used the resource fraction (in Eqn. 20) is expressed as a volume fraction similar to that of the homgoeneous case, and following the same theory the resource fraction is calculated as follows.

$$\int_\Omega \frac{M(\boldsymbol{x})}{M_0} d\Omega = \frac{1}{N_e} \sum_{e=1}^{N_e} x_{0,e} \tag{24}$$

Note that this constraint is evaluated purely based on $x_{0,e}$ and so elements with a higher Young's modulus have the same cost as those with a lower Young's modulus. However, when a modulus constraint is used, elements of a higher Young's modulus come at a greater cost than those of a lower Young's modulus. This encourages designs with a wider spectrum of Young's modulus values. The resource fraction is calculated by Eqn. 25 when a modulus constraint is used.

$$\int_\Omega \frac{M(\boldsymbol{x})}{M_0} d\Omega = \frac{1}{N_e E_u} \sum_{e=1}^{N_e} E_e \tag{25}$$

Penalization is a common practice in topology optimization as it eliminates greyscale, caused by intermediate densities in converged designs. However there are other irregularities that can appear in optimized design that also need attention. One such irregularity is checkerboarding. Checkerboarding can occur when using 4-node quadrilateral elements. These elements allow load to be transferred from one element to another diagonally through a single common node which can cause the off-diagonal elements to become void. Hence, an infeasible geometry is created as there will be 0 thickness at the common node. If this occurs multiple times within the structure a solid-void checkered pattern is produced which gives rise to the name. To ensure this does not occur a density filter is used [20]. Density filters alter the density of each element by producing a relationship between an element's material density and the material density of its surrounding elements. A density filter matrix, $\boldsymbol{W}$ is defined such that

$$\tilde{\boldsymbol{x}} = \boldsymbol{W}\boldsymbol{x} \tag{26}$$

where $\tilde{\boldsymbol{x}}$ is the filtered or physical variables and $\boldsymbol{x}$ is referred to as the independent variables. For the homogeneous case, these variables are the material densities, whereas in the FGM case, the variables are both material densities and mixing ratios. In the FGM case Young's modulus, E, is also filtered to ensure smooth gradations throughout the structure. Note that when using a modulus constraint only E is filtered and not the design variables. Physical variables produce the final structure and are used in FEA, whereas the sensitivities are calculated with respect to the independent variables. A filter radius, r, is used to determine how many of the surrounding elements will contribute to the density filter. For any element, e, a circle of radius r is traced with its center at e's centroid. All other elements whose centroid lie within this radius contribute to the material density of e. Element contributions are weighted such that the closer the neighboring element the higher the weighting will be. There is a linear relationship between the weighting and the distance between element centroids. All elements outside the filter radius carry no weight. This relationship can be represented as a cone with its center coincident to the centroid of e and the weighting of other elements is defined by the height of the cone above their respective centroid, see Figure 4. The entries in $\boldsymbol{W}$, w_{ij}, are calculated as

$$\bar{w_{ij}} = \max[0, r - d_{ij}] \tag{27}$$

$$w_{ij} = \frac{1}{\sum_{k=1}^{N_r} \bar{w_{ij,k}}} \bar{w_{ij}} \tag{28}$$

where the subscript ij denotes the i^{th} row and j^{th} column, r is the filter radius and d_{ij} is the distance between the two element centroids, N_r is the number of elements whose centroids lie within the filter radius. Eqn. 28 normalizes the entries of $\boldsymbol{W}$ calculated in Eqn. 27 such that the rows of $\boldsymbol{W}$ sum to 1.

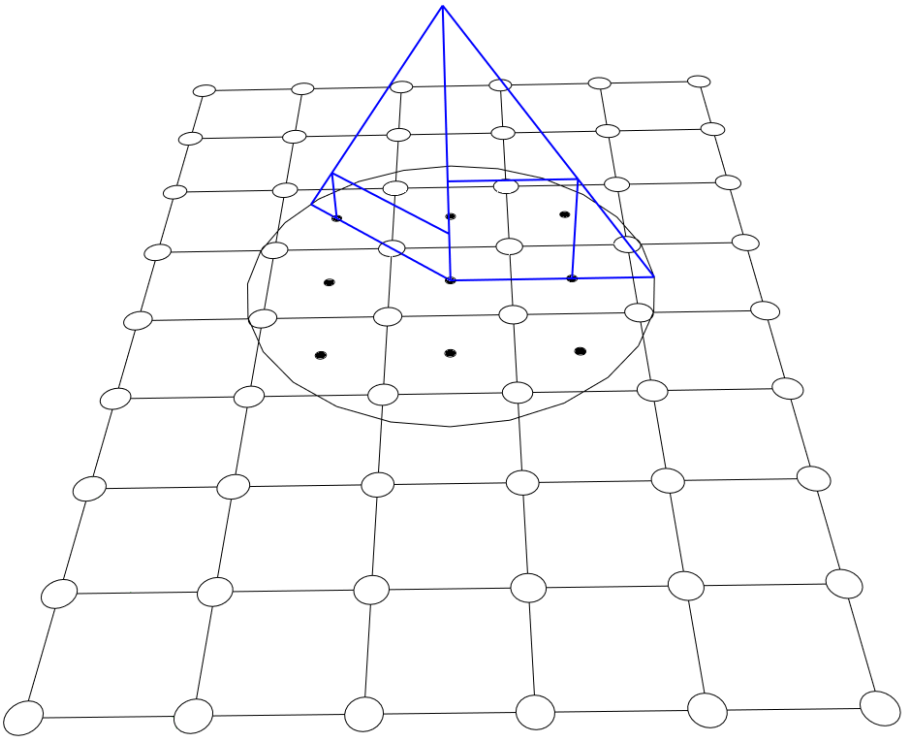

Fig. 4: Cone representation of the filtering process.

3.3 Sensitivity Analysis

Sensitivities were captured using the adjoint method, the formula for which is derived below. First the objective function is expressed in augmented Lagrangian form.

$$\Pi = g + \boldsymbol{\lambda}^{\mathrm{T}}\mathbf{R} = g + \begin{bmatrix} \boldsymbol{\lambda}_f{}^{\mathrm{T}} & \lambda_p{}^{\mathrm{T}} \end{bmatrix} \begin{bmatrix} \mathbf{R}_f \\ \mathbf{R}_p \end{bmatrix} \tag{29}$$

where $\boldsymbol{\lambda}$ is the Lagrangian multiplier, whose values must be determined. However, note that for any $\boldsymbol{\lambda}$, $\Pi = g$ as we know $\mathbf{R} = 0$. This equation can also be represented in terms of free and prescribed degrees of freedom denoted by the subscripts f and p respectively. We require the sensitivities of the objective function with respect to each design variable. These sensitivities can now be represented in vector form as the derivative of Π. Using the chain rule we obtain the expression

$$\begin{aligned} \frac{d\Pi}{d\boldsymbol{x}} = \frac{\partial g}{\partial \boldsymbol{x}} + \frac{\partial g}{\partial \mathbf{u}_f}\frac{d\mathbf{u}_f}{d\boldsymbol{x}} + \frac{\partial g}{\partial \theta}\frac{d\theta}{d\boldsymbol{x}} + \boldsymbol{\lambda}_f{}^{\mathrm{T}}\left[\frac{\partial \mathbf{R}_f}{\partial \boldsymbol{x}} + \frac{\partial \mathbf{R}_f}{\partial \mathbf{u}_f}\frac{d\mathbf{u}_f}{d\boldsymbol{x}} + \frac{\partial \mathbf{R}_f}{\partial \theta}\frac{d\theta}{d\boldsymbol{x}}\right] \\ + \lambda_p{}^{\mathrm{T}}\left[\frac{\partial \mathbf{R}_p}{\partial \boldsymbol{x}} + \frac{\partial \mathbf{R}_p}{\partial \mathbf{u}_f}\frac{d\mathbf{u}_f}{d\boldsymbol{x}} + \frac{\partial \mathbf{R}_p}{\partial \theta}\frac{d\theta}{d\boldsymbol{x}}\right] \end{aligned} \tag{30}$$

Together, θ and $\mathbf{u}_f$ are the solutions to the finite element analysis. Note that some of the terms on the right hand side of Eqn. 30 have no dependence on the parameter they are differentiated with respect to, and so are equal to zero (first, second, and eighth terms). Note also the difference between $\frac{\partial}{\partial \boldsymbol{x}}$ and $\frac{d}{d\boldsymbol{x}}$ operators, which represent explicit and implicit derivatives respectively. Explicit derivatives capture only direct dependence of the function,

whereas the implicit derivatives also capture indirect dependence due to the solution of the equilibrium equation. We seek a $\boldsymbol{\lambda}$ that causes all implicit terms to vanish. This yields

$$\begin{aligned} {\lambda_p}^{\mathrm{T}} &= -\frac{\partial g}{\partial \theta} \\ {\boldsymbol{\lambda}_f}^{\mathrm{T}} &= -{\lambda_p}^{\mathrm{T}} \frac{\partial \mathbf{R}_p}{\partial \mathbf{u}_f} \left[\frac{\partial \mathbf{R}_f}{\partial \mathbf{u}_f} \right]^{-1} = -{\lambda_p}^{\mathrm{T}} \boldsymbol{K}_{pf} \boldsymbol{K}_{ff}^{-1} \end{aligned} \tag{31a}$$

$$\begin{aligned} {\lambda_p}^{\mathrm{T}} &= \mathbf{0} \\ {\boldsymbol{\lambda}_f}^{\mathrm{T}} &= -\frac{\partial g}{\partial \mathbf{u}_f} \left[\frac{\partial \mathbf{R}_f}{\partial \mathbf{u}_f} \right]^{-1} = -\frac{\partial g}{\partial \mathbf{u}_f} \boldsymbol{K}_{ff}^{-1} \end{aligned} \tag{31b}$$

where Eqn. 31a and 31b are for objective functions of mechanical and geometric advantage respectively. The tangent stiffness matrix, $\boldsymbol{K}_{tan}$, is also partitioned where $\boldsymbol{K}_{pf}$ is the matrix whose rows and columns are equal to the prescribed and free degrees of freedom of $\boldsymbol{K}_{tan}$. Likewise $\boldsymbol{K}_{ff}$ is the matrix whose rows and columns are equal free-free degrees of freedom of $\boldsymbol{K}_{tan}$. The final adjoint sensitivity then becomes

$$\begin{aligned} \frac{d\Pi}{d\boldsymbol{x}} &= {\lambda_p}^{\mathrm{T}} \frac{\partial \mathbf{R}_p}{\partial \boldsymbol{x}} + {\boldsymbol{\lambda}_f}^{\mathrm{T}} \frac{\partial \mathbf{R}_f}{\partial \boldsymbol{x}} = {\boldsymbol{\lambda}}^{\mathrm{T}} \frac{\partial \mathbf{R}}{\partial \boldsymbol{x}} \\ \implies \frac{d\Pi}{dx_e} &= {\boldsymbol{\lambda}_e}^{\mathrm{T}} \frac{\partial \mathbf{R}}{\partial x_e} \end{aligned} \tag{32}$$

where $\boldsymbol{\lambda}$ and $\boldsymbol{\lambda}_e$ can contain entries from both fixed and prescribed degrees of freedom. The external force has no direct dependence on $\boldsymbol{x}$, therefore the derivative of the residual with respect to $\boldsymbol{x}$ is equal to the negative of the internal force differentiated with respect to $\boldsymbol{x}$.

$$\begin{aligned} \frac{\partial \mathbf{R}}{\partial x} &= -\frac{\partial}{\partial x} \left(\int_{\Omega_e} \bar{\mathbf{B}}^{\mathrm{T}} \bar{\boldsymbol{\sigma}} d\Omega_e \right) \\ \frac{\partial \mathbf{R}}{\partial x} &= -p x^{p-1} \int_{\Omega_e} \bar{\mathbf{B}}^{\mathrm{T}} \left(\frac{1}{J} \left[\lambda_0 [\ln J] \mathbf{I} + \mu_0 (\mathbf{B} - \mathbf{I}) \right] \right) \end{aligned} \tag{33}$$

3.4 Optimization Algorithm

The optimization problem is solved using a gradient-based algorithm, namely the Method of Moving Asymptotes (MMA), outlined in [35]. The deisgn problem is said to have reached an optimal solution once the Karush-Kuhn-Tucker (KKT) conditions are satisfied to a tolerance of 10^{-3} [36], [37]. The complete algorithm combines methods discussed in sections 2 and 3. This algorithm is represented by the flowchart in Figure 5.

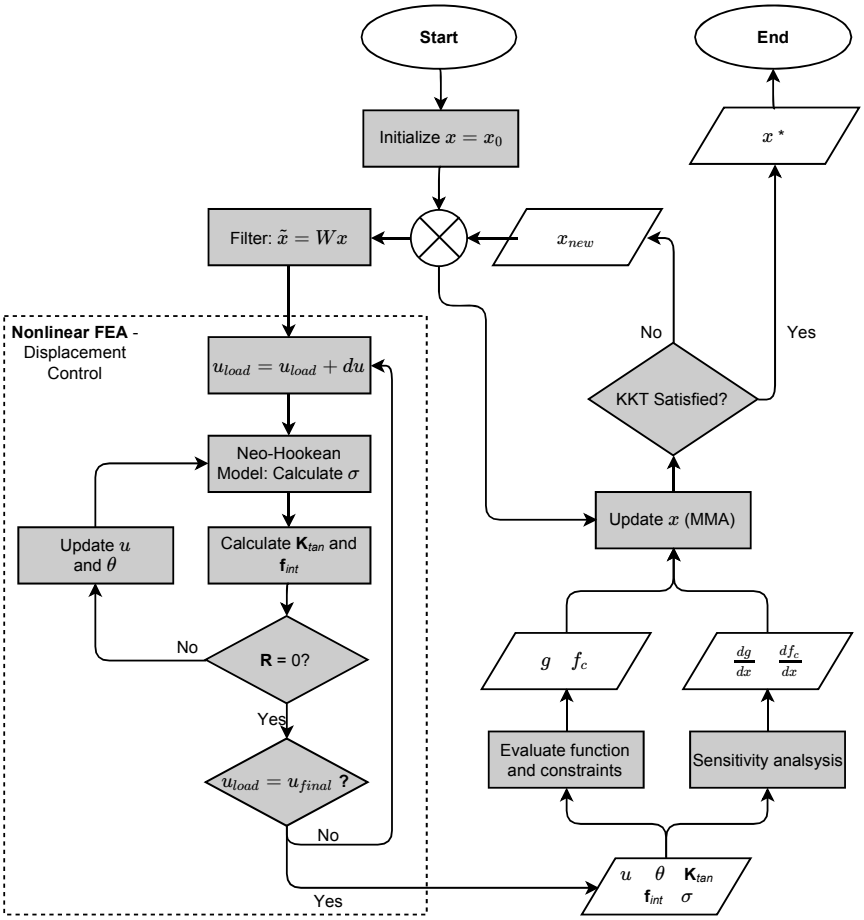

Fig. 5: Flowchart of the complete algorithm used in this analysis.

3.5 Post-Optimization Analysis

Once designs have converged to an optimal structure the von Mises stress is calculated for each element to give a better understanding of how stress is distributed throughout the mechanism. Also, comparing the maximum von Mises stress in each homogeneous mechanism to that of the FGM mechanisms will show how stress concentrations can be reduced. The von Mises stress is calculated at the 4 Gauss points of an element and averaged to obtain the von Mises stress within the element. The von Mises stress can be defined in terms of plane stress as

$$\sigma_{VM} = \sqrt{{\sigma_{11}}^2 - \sigma_{11}\sigma_{22} + {\sigma_{22}}^2 + 3{\sigma_{12}}^2} \tag{34}$$

where σ_{VM} is the von Mises stress for a single element and σ_{ij} is the i^{th} row and j^{th} column of the Cauchy stress for that element, as calculated in Eqn. 10.

4 Materials Testing

To conduct the mechanical analysis described in section 2 we require the Young's modulus, E, and the Poisson's ratio, ν. The material properties used in the mechanical analysis were based on materials available for prototyping. Prototypes will be created using a Polyjet 3D printer by Stratasys (Objet260 Connex3). Two Stratasys materials are modeled, TangoBlack+ and a material blend of TangoBlack+, RGD531 and RGD515 (digital material code FLX95595). Both materials experience geometric nonlinearity however material 1 (TangoBlack+) is an extremely flexible, compliant material whereas material 2 (blend FLX95595) is a much stiffer material. The homogeneous model will be based on material 2 only (stiffer material) whereas the FGM model will be able to use any mixing ratio of the two materials.

The Young's modulus for both materials is obtained through simple tensile tests in accordance with ASTM standard D638 [38]. Based on mean values of 6 samples, material 1 was found to have a Young's modulus of 0.14 MPa, and material 2, a Young's modulus of 11 MPa. The Poisson's ratio was found by extending the sample in the axial direction in small incremental steps whilst remaining within the linear elastic region. At each increment the deformation in axial and transverse directions were recorded and used to calculate strains, $\varepsilon_{x,y,z}$. Poissons ratio, by definition, is then calculated as

$$\nu = -\frac{d\varepsilon_x}{d\varepsilon_z} = -\frac{d\varepsilon_y}{d\varepsilon_z} \tag{35}$$

where ε_z is axial strain, and ε_x and ε_y are the transverse strains. Poisson's ratio was assumed to be constant for both materials and based on mean values of 6 readings was found to be 0.4.

5 Results

5.1 Case a: Gripper problem

Each gripper problem is solved for a unit input displacement (1 mm) and a larger displacement equal to 8% the design domain length (5 mm). Firstly the mechanical analysis problem is solved for the homogeneous case (whether the problem itself is homogeneous or functionally graded) with all element densities equal and a resource fraction of $\bar{M}$. Under this scenario the compliance of the structure is calculated and taken to be the minimum possible value of compliance, C_{min} (refer to Eqn. 20). All gripper results are presented with a resource constraint, $\bar{M}$, of 0.4. The design problem is detailed in Figure 3a and has an objective function to maximize mechanical advantage. Functionally graded mechanisms were modeled in two different ways – firstly a volume constraint is used which only accounts for $\boldsymbol{x}_0$, and secondly we implemented a modulus constraint which accounts for values of both $\boldsymbol{x}_0$ and $\boldsymbol{x}_1$ (refer to Eqn. 23). All mechanisms have a Poisson's ratio of 0.4 with a Young's modulus of 11 MPa for homogeneous designs, while the local Young's modulus is optimally varied between 0.14 MPa and 11 MPa for FGM designs. Figures 6 and 7 show results for gripper designs with 1 mm and 5 mm input displacements respectively. Table 1 compares the mechanical advantage and maximum von Mises stress for all 6 gripper designs. Convergence of the KKT norm and mechanical advantage for each gripper design is shown in Figure 8.

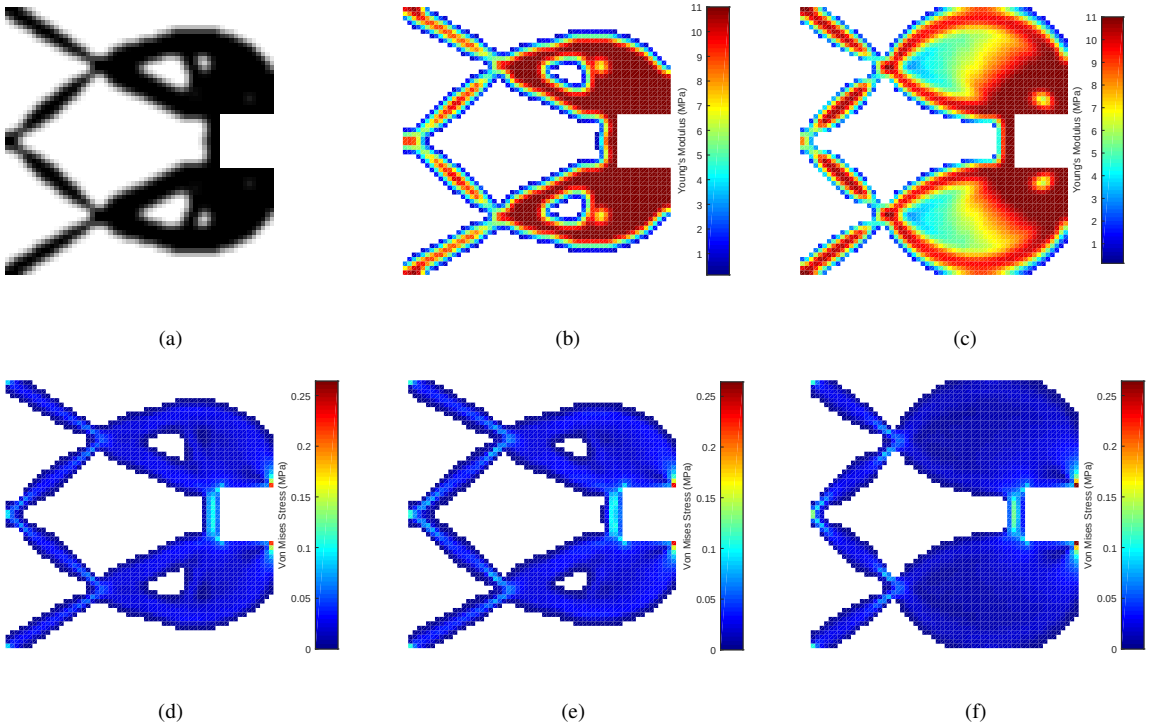

Fig. 6: Gripper results for 1 mm input displacement. Converged topologies are shown on top – (a) homogeneous design, (b) FGM design with a volume constraint, (c) FGM design with a Young's modulus constraint. Von Mises stress distributions are shown on bottom – (d) homogeneous design, (e) FGM design with a volume constraint, (f) FGM design with a Young's modulus constraint.

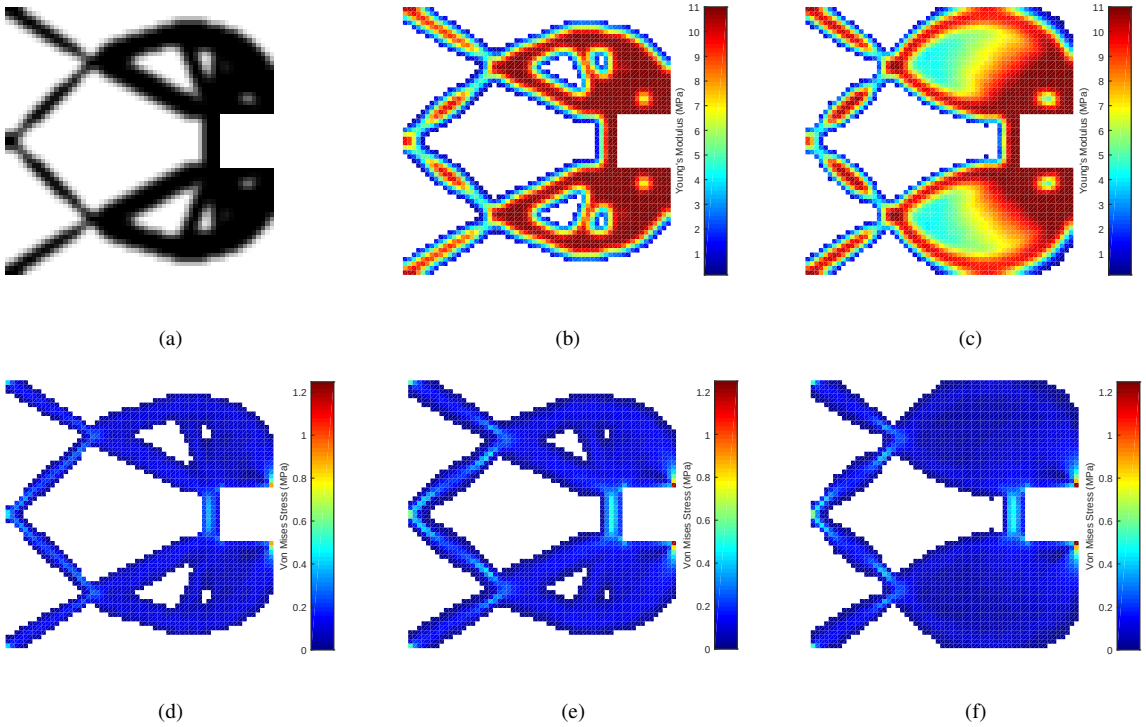

Fig. 7: Gripper results for 5 mm input displacement. Converged topologies are shown on top – (a) homogeneous design, (b) FGM design with a volume constraint, (c) FGM design with a Young's modulus constraint. Von Mises stress distributions are shown on bottom – (d) homogeneous design, (e) FGM design with a volume constraint, (f) FGM design with a Young's modulus constraint.

Material	u_{in} *(mm)*	*Constraint*	*Mech. Adv.*	*Max VM (MPa)*
Homogeneous	1	-	2.26	0.216
FGM	1	Volume	2.20	0.232
FGM	1	Modulus	2.55	0.264
Homogeneous	5	-	1.93	0.881
FGM	5	Volume	2.34	1.177
FGM	5	Modulus	2.59	1.248

Table 1: Comparisons between mechanical advantage and maximum von Mises stress in inverter results.

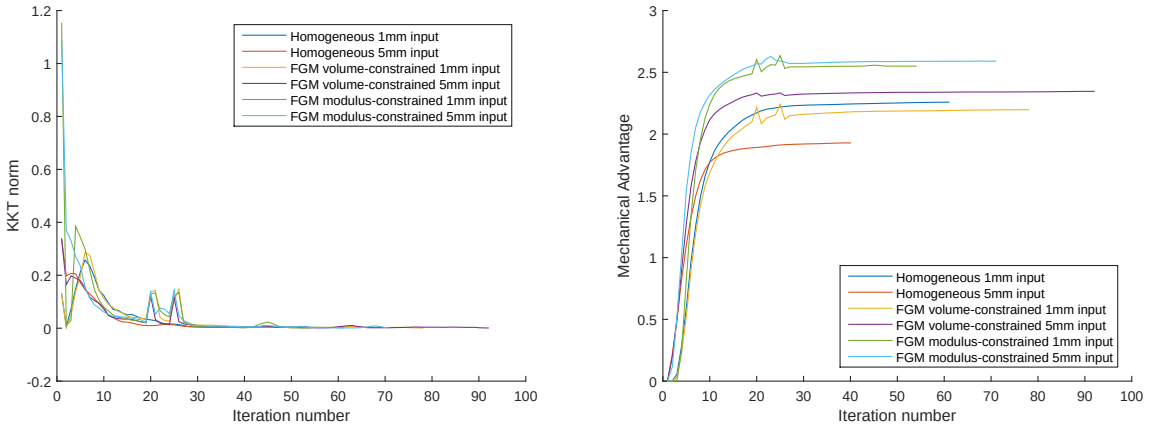

(a) (b)

Fig. 8: Convergence plots of (a) KKT norm and (b) mechanical advantage for each gripper design

When the gripper problem is optimized for small displacements we see no major difference in mechanical advantage between the volume-constrained gripper and homogeneous gripper. However, the modulus-constrained gripper out-performs both with a mechanical advantage that is 14% larger. For large displacement grippers, both FGM grippers achieve a higher mechanical advantage than the homogeneous design with volume- and modulus-constrained mechanisms producing 21% and 34% higher mechanical advantages respectively. In all cases, the FGM mechanisms also experienced a higher maximum von Mises stress. By comparing the final topologies we see that the homogeneous and volume-constrained grippers are similar, whereas the the topology of the modulus-constrained gripper is distinctively different.

From the stress distributions we see that for all gripper designs the highest von Mises stress occurs at the output and the second highest at the input and boundary conditions. These stress concentrations are prominent in all designs and are an unavoidable for the mechanical advantage problem. The other stress concentration occur at the back of the gripper's jaws and at the complaint joints, as seen in all examples. By comparing stress concentrations for each design problem we see that higher magnitudes of stress are produced in FGM mechanisms compared to the homogeneous designs. Stresses in other structural members appear to be lowest in the modulus-constrained designs, which is expected as more compliant materials are used.

5.2 Case b: Inverter problem

The inverter problem is solved for a unit input displacement (1 mm) and a larger displacement equal to 8% of the design domain length (5 mm). Similarly to the gripper problem, the analysis is first conducted on the homogeneous mechanism to obtain the value C_{min}. All inverter results are presented with a resource constraint of 0.3. The design problem is detailed in Figure 3b and has an objective function as to maximize geometric advantage. Material properties are the same for the inverter and gripper designs – Poisson's ratio of 0.4, homogeneous mechanisms are modeled with a Young's modulus of 11 MPa, and FGM mechanisms with a Young's modulus optimally varied between 0.14 MPa and 11 MPa based on location within the mechanism. Figures 9 and 10 show results for 1 mm and 5 mm input displacements respectively. Table 2 compares the geometric advantage and maximum von Mises stress for all 6 inverter designs.

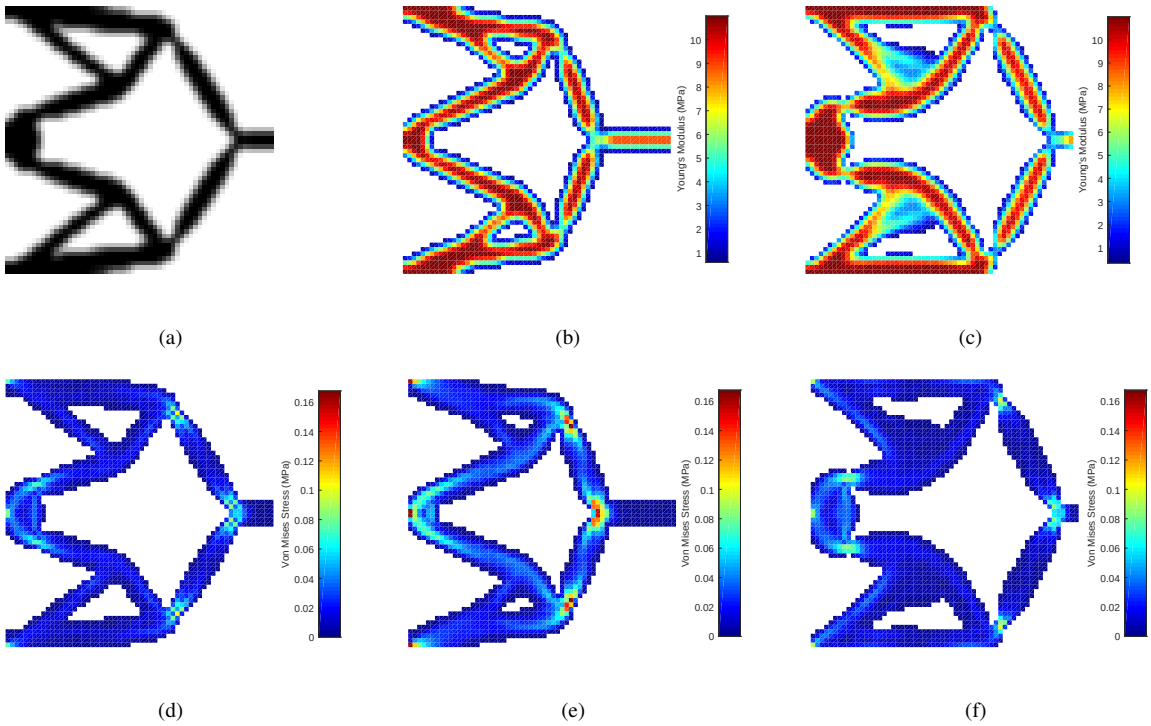

Fig. 9: Inverter results for 1 mm input displacement. Converged topologies are shown on top – (a) homogeneous design, (b) FGM design with a volume constraint, (c) FGM design with a Young's modulus constraint. Von Mises stress distributions are shown on bottom – (d) homogeneous design, (e) FGM design with a volume constraint, (f) FGM design with a Young's modulus constraint.

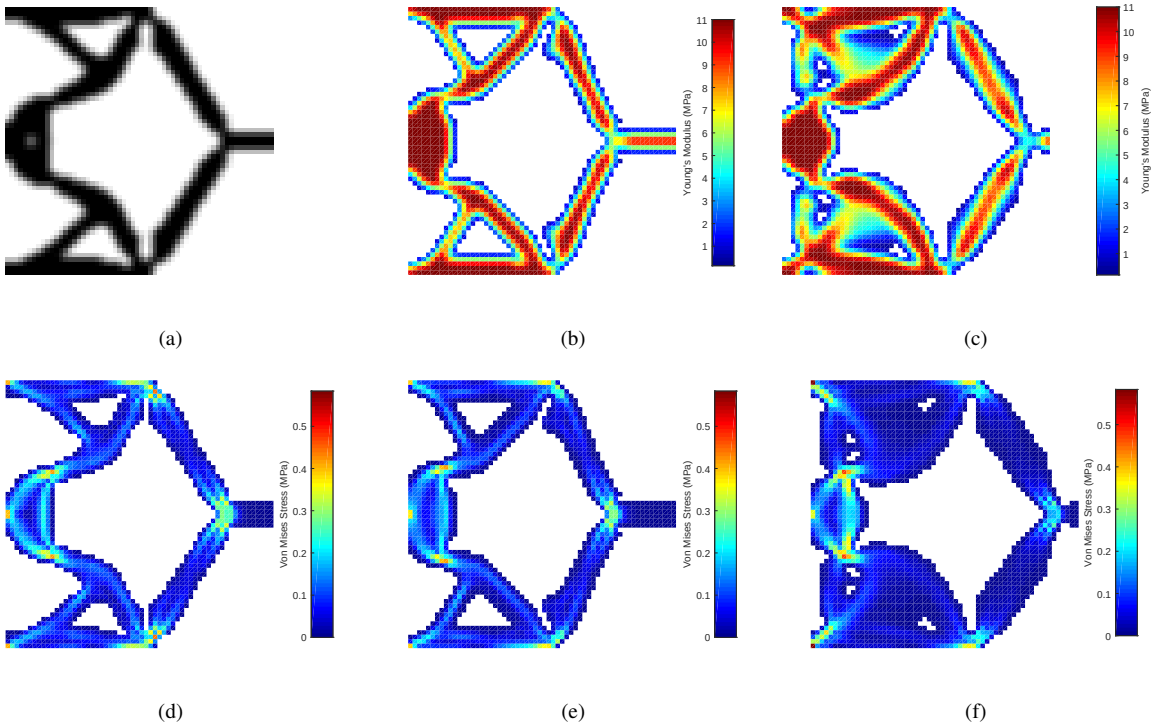

Fig. 10: Inverter results for 5 mm input displacement. Converged topologies are shown on top – (a) homogeneous design, (b) FGM design with a volume constraint, (c) FGM design with a Young's modulus constraint. Von Mises stress distributions are shown on bottom – (d) homogeneous design, (e) FGM design with a volume constraint, (f) FGM design with a Young's modulus constraint.

Material	u_{in} *(mm)*	*Constraint*	*Geo. Adv.*	*Max VM (MPa)*
Homogeneous	1	-	1.39	0.103
FGM	1	Volume	1.93	0.168
FGM	1	Modulus	2.32	0.098
Homogeneous	5	-	1.09	0.445
FGM	5	Volume	1.46	0.412
FGM	5	Modulus	1.45	0.583

Table 2: Comparisons between geometric advantage and maximum von Mises stress in inverter results.

FGM mechanisms produce higher geometric advantages compared to the homogeneous mechanisms. For small displacements the volume- and modulus-constrained mechanisms produced geometric advantages 38% and 67% higher than the homogeneous mechanism. For these designs, the volume-constrained mechanism saw the highest maximum von Mises stress, with the modulus-constrained and homogeneous mechanisms experiencing similar maximum stress values. When designed for large displacements, both FGM mechanisms produced a similar geometric advantage that is 25% higher than the homogeneous design. However, there is a larger difference in maximum von Mises stress. The modulus-constrained design experienced the largest stress at 31% higher than the homogeneous design, and the volume-constrained mechanism, the smallest at 7% lower than the homogeneous design. From the stress distributions we see that inverter designs experience stress concentrations at the input location, fixed supports, and compliant joints. Implementing FGMs seems to have little beneficial impact on the stress distributions in the inverter mechanisms.

Based the results of both design problems it can be said that by varying the material properties throughout the design domain, higher mechanical/geometric advantages can be produced. However, as the algorithm is optimizing to maximize the mechanical/geometric advantage, the optimizer does not take into account the magnitude of the stress. As a result, we have seen here that FGM designs can experience higher stresses, which should be considered

for future designs.

We can also compare these results to two-material designs. Two-material designs were created using a three-phase topology optimization method detailed in [12] and [39]. Two-material gripper and inverter designs, and their respective stress distributions, are shown below in Figure 11. Gripper and inverter designs are produced with volume constraints of 0.4 and 0.3 respectively. The three-phase topology optimization method utilizes a volume constraint on each material. Both designs are produced with a 7:3 ratio of stiff to complaint material with Young's modulus values of 11 MPa and 0.14 MPa respectively, i.e. the upper and lower Young's modulus bounds for FGM designs. Both two-material designs are also solved for an input displacement of 5 mm.

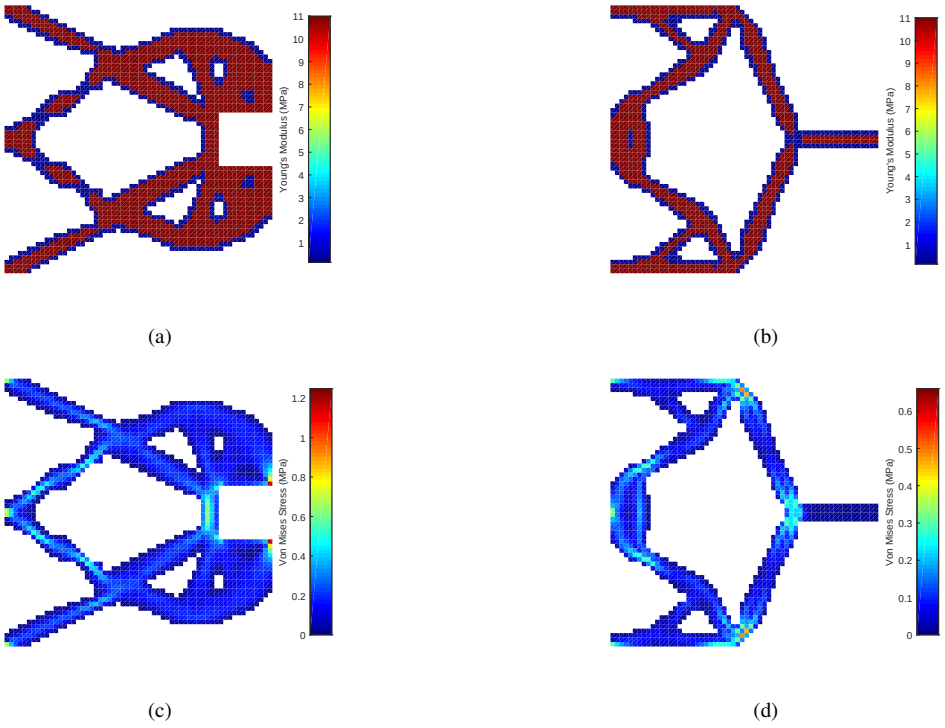

(a) (b)

(c) (d)

Fig. 11: Two-material results for 5 mm input displacement. Converged topologies are shown on top – (a) gripper design, (b) inverter design, (c) gripper stress distribution, (d) inverter stress distribution.

The two-material gripper design produced a mechanical advantage of 2.27 and experienced a maximum von Mises stress of 1.182 MPa. This means that the two-material gripper produces a mechanical advantage 18% higher than the homogeneous designs. However, compared to FGM designs the two-material gripper produces a mechanical advantage 3% lower than the volume-constrained design and 14% lower than the modulus constrained design. The two-material gripper experienced similar stress distributions to the grippers previously presented. The maximum von Mises stress is similar to the volume-constrained FGM mechanism and so it is also lower than that of the modulus constrained mechanism.

The two-material inverter design produced a geometric advantage of 1.32 and experienced a maximum von Mises stress of 0.491 MPa. This geometric advantage is 9% lower than the FGM inverter mechanisms but 21% higher than the homogeneous mechanisms. There is little difference in the stress distributions, however, the maximum von Mises stress is higher than the volume-constrained mechanism and lower than the modulus-constrained mechanism. Based on the results for both design problems we have found that two-material mechanisms perform better than homogeneous designs which is in keeping with previous findings presented in literature, [8] to [14]. However, we have also found that using FGMs can lead to designs that are more efficient than the two-material mechanisms.

6 Conclusion

This paper presented the hypothesis that implementing functionally graded materials into the design of compliant mechanisms will produce more efficient designs through increasing mechanical/geometric advantage and improving stress distributions. Two design studies have been presented, a gripper problem which optimizes for mechanical advantage and an inverter problem which optimizes for geometric advantage. In all cases we have found that by using FGMs, higher mechanical/geometric advantages can be achieved compared to the traditional homogeneous designs. Stress concentrations are still present in the converged FGM designs and the majority of these mechanisms experienced a higher maximum von Mises stress than the homogeneous designs. In this work we did not consider stresses during the optimization process, but calculated stresses in the converged designs. Future work will include stress considerations during the optimization process to ensure a reduction in von Mises stress. We also found that FGM mechanisms can produce higher mechanical/geometric advantages than two-material mechanisms, which have previously been shown to be more efficient than homogeneous designs. We therefore conclude that implementing FGMs into compliant mechanism designs has a positive impact on the mechanism's structural performance. Future work will further investigate the range of the advantages that can be achieved by using FGMs through: solving new design problems; integrating stress limiting criterion into the optimization process to ensure reduction of stress concentrations; fabricating converged designs, and experimentally validating computational results.

References

1. O. Sigmund, "On the Design of Compliant Mechanisms Using Topology Optimization" Mechanics of Structures and Machines: An International Journal, vol. 25, no. 4, pp. 493-542, 1997.
2. J. Buck, T Mc Mahon, D. Huot, "Space Station 3-D Printer Builds Ratchet Wrench To Complete First Phase Of Operations," 22 Dec. 2014. [Online]. Available: `https://www.nasa.gov/mission_pages/station/research/news/3Dratchet_wrench`. [Accessed 12/12/2016].
3. T. J. Prater, Q. A. Bean, R. D. Beshears, T. D. Rolin, N. J. Werkheiser, E. A. Ordonez, R. M. Ryan, F. E. Ledbetter III, "Summary Report on Phase I Results from the 3D Printing in Zero G Technology Demonstration Mission, Volume I," NASA Technical Reports Server, Jul. 1st 2016.
4. OpenStax, "Anatomy & Physiology", OpenStax, 2013.
5. A. Marin, A. A. Fuentes, "Human Bone: Functionally Graded Material Structures with Complex Geometry and Loading," Department of Mechanical Engineering, University of Texas-Pan American.
6. D. Wolf, S. Yip, "Material Interfaces: Atomic-level Structure and Properties," Netherlands: Springer, 1993.
7. Y. Miyamoto, W. A. Kaysser, B. H. Rabin, A. Kawasaki, R. G. Ford, "Functionally Graded Materials: Design, Processing and Applications," Springer, 1999.
8. C. Alonso, "Topology synthesis of multi-material complaint mechanisms with Sequential Element Rejection and Admission," Finite Elements in Analysis and Design, vol. 85, pp. 11-19, 2014.
9. L. Yin, G. K. Ananthasuresh, "Topology optimization of compliant mechanisms with multiple materials using a peak function material interpolation scheme," Structural and Multidisciplinary Optimization, vol. 23, no. 1, pp. 49-62, 2003.
10. M. P. Bendsoe, O. Sigmund, "Material interpolation schemes in topology optimization," Archive of Applied Mathematics, vol. 69, pp. 635-654, 1999.
11. O. Sigmund, "Design of multiphysics actuators using topology optimization Part II: Two-material structures," Computer Methods in Applied Mechanics, vol. 190, no. 49-50, pp. 6605-6627, 2001.
12. O. Sigmund, S. Torquato, "Design of materials with extreme thermal expansion using a three-phase topology optimization method," Journal of the Mechanics and physics of Solids, vol. 45, no. 6, pp. 1037-1067, 1997.
13. J. Stegmann, E. Lund, "Discrete material optimization of general shell structures," International Journal for Numerical Methods in Engineering, vol. 62, no. 14, pp. 2009-2027, 2005.
14. A. Gaynor, N. A. Meisel, C. B. Williams, J. K. Guest, "Multiple-Material Topology Optimization of Compliant Mechanisms Created via Polyjet Three-Dimensional Printing," Journal of Manufacturing Science and Engineering, vol. 136(6), 2014.
15. R. C. Carbonari, G. H. Paulino, E. C. N. Silva, "Integral Piezoactuator with Optimum Placement of Functionally Graded Material - A Topology Optimization Paradigm," Journal of Intelligent Material Systems and Structures, vol. 21, no. 16, pp. 1653-1668, 2010.
16. R. C. Carbonari, E. C. N. Silva, G. H. Paulino, "Multi-actuated functionally graded piezoelectric micro-tools design: A multiphysics topology optimization approach," International Journal for Numerical Methods in Engineering, vol. 77, no. 3, pp. 301-336, 2009.
17. L. Yin, G. K. Ananthasuresh, "A novel topology design scheme for the multi-physics problems of electro-thermally actuated compliant micromechanisms," Sensors and Actuators A: Physical, Vols. 97-98, pp. 599-609, 2002.
18. Q. Xia, M. Yu Wang, "Simultaneous optimization of the material properties and the topology of functionally graded structures," Computer-Aided Design, ACM Symposium on Solid and Physical Modeling and Applications, vol. 40, no. 6, pp. 660-675, 2008.
19. F. V. Stump, E. C. N. Silva, G. H. Paulino, "Optimization of material distribution in functionally graded structures with stress constraints," Communications in Numerical Methods in Engineering, vol. 23, no. 6, pp. 535-551, 2007.
20. T. E. Bruns, D. A. Totorelli, "Topology optimization of non-linear structures and compliant mechanisms," Computer Methods in Applied Mechanics and Engineering, vol. 190, no. 26-27, pp. 3443-3459, 2001.
21. C. B. W. Pedersen, T. Buhl, O. Sigmund, "Topology synthesis of large-displacement complaint mechanisms," Numerical Methods in Engineering, vol. 50, no. 12, pp. 2683-2705, 2001.
22. H. C. Gea, J. Luo, "Topology optimization of structures with geometrical nonlinearities," Computers & Structures, vol. 79, no. 20-21, pp. 1977-1985, 2001.
23. N. H. Kim, "Introduction to Nonlinear Finite Element Analysis," New York: Springer US, 2015.

24. P. Wriggers, “Nonlinear Finite Element Methods,” Springer, Berlin Heidelberg, 2008.
25. K. A. James, H. Waisman, “Layout design of a bi-stable cardiovascular stent using topology optimization,” Computer Methods in Applied Mechanics and Engineering, vol. 305, pp. 869-890, 2016.
26. A. S. Ramos Jr., G. H. Paulino, “Convex topology optimization for hyperelastic trusses based on the ground-structure approach,” Structural and Multidisciplinary Optimization, vol. 51, no. 2, pp. 287-304, 2015.
27. F. A. Gomes, T. A. Senne, “An algorithm for the topology optimization of geometically nonlinear structures,” International Journal for Numerical Methods in Engineering, 2014.
28. Y. Lou, M. Li, Z. Kang, “Topology optimization of hyperelastic structures with frictionless contact supports,” International Journal of Solids and Structures, vol. 81, pp. 373-382, 2016.
29. T. Belytschko, W. K. Liu, B. Moran, K. Elkhodary, “Nonlinear Finite Elements for Continua and Structures,” Wiley, Chichester, West Sussex, UK, 2002.
30. Y. Basar, D. Weichert, “Nonlinear Continuum Mechanics of Solids: Fundamental Mathematical and Physical Concepts,” Springer-Verlag, Berlin Heidelberg, 2000.
31. G. Marckmann and E. Verron, “Comparison of Hyperelastic Models for Rubber-Like Materials,” Rubber Chemistry and Technology, vol. 79, no. 5, pp. 835-858, 2006.
32. J. L. Batoz, G, Dhatt, “Incremental displacement algorithms for nonlinear problems,” International Journal for Numerical Methods in Engineering, vol. 14, no. 8, pp. 1262-1267, 1979.
33. M. Zhou, G. I. N. Rozvany, “The COG algorithm, Part II: Topological, geometrical and generalized shape optimization,” Computer Methods in Applied Mechanics and Engineering, vol. 89, no. 1-3, pp. 309-336, 1991.
34. M. P. Bendse, “Optimal shape design as a material distribution problem,” Structural optimization, vol. 1, no. 4, pp. 193-202, 1989.
35. K. Svanberg, “The method of moving asymptotes — a new method for structural optimization,” International Journal for Numerical Methods in Engineering, vol. 24, no. 2, pp. 359-373, 1987.
36. H. Kuhn, A. Tucker, “Nonlinear Programming,” in Proceedings of 2nd Berkeley Symposium, Berkeley, CA, 1951.
37. W. Karush, “Minima of functions of several variables with inequalities as side constraints,” Master’s Thesis, University of Chicago, Chicago, IL, 1939.
38. “ASTM D638-14 Standard Test Method for Tensile Properties of Plastics,” ASTM International, 2014.
39. O. Sigmund, S. Torquato, “Design of smart composite materials using topology optimization,” Smart Materials and Structures, vol. 8, no. 3, pp. 365-379, 1999.
40. T. Zegard, G. H. Paulino, “Bridging topology optimization and additive manufacturing,” Structural and Multidisciplinary Optimization, vol. 53, no. 1, pp. 175-192, 2016.
41. N. Coburn, P. G. Hodge, “Theory of Perfectly Plastic Solids,” Mathematics Magezine, vol. 27, no. 4, pp. 231-232, 1954.
42. G. A. Holzapfel, “Nonlinear Solid Mechanics: A Continuum Approach for Engineering Science,” New York: John Wiley & Sons, 2000.
43. C. Alonso, O. M. Querin, R. Ansola, “A Sequential Element Rejection and Admission (SERA) method for compliant mechanisms design,” Structural and Multidisciplinary Optimization, Springer-Verlag, Berlin, 2013.
44. G. Udupa, S. S. Rao, K. V. Gangadharan, “Functionally Graded Composite Materials: An Overview,” Procedia Materials Science, Elsevier, vol. 5, pp. 1291-1299, 2014.
45. O. Sigmund, J. Petersson, “Numerical Instabilities in Topology Optimization A Survey on Procedures Dealing with Checkerboards, Mesh Dependencies and Local Minima,” Structural Optimization, Springer-Verlag, 1998.
46. M. P. Bendse, O. Sigmund, “Topology Optimization: Theory, Methods and Applications,” Berlin Heidelberg: Springer-Verlag, 2004.
47. A. Saxena, “Topology Design of Large Displacement Compliant Mechanisms with Multiple Materials and Multiple Output Ports,” Structural Multidisciplinary Optimization, Spring-Verlag, 2005.
48. O. Sigmund, “A 99 Line Topology Optimization Code Written in Matlab,” Structural Multidisciplinary Optimization, Springer-Verlag, 2001.
49. S. R. M. Almeida, G. H. Paulino, E. C. N. Silva, “Layout and material gradation in topology optimization of functionally graded structures: a globallocal approach,” Structural and Multidisciplinary Optimization, vol. 42, no. 6, pp. 855-868, 2010.
50. N. Vermaak, G. Michailidis, G. Parry, R. Estevez, G. Allaire, Y. Brechet, “Material interface effects on topology optimization of multi-phase structures using a level set method,” Structural and Multidisciplinary Optimization, vol. 50, no. 4, pp. 623-644, 2014.